Computational Materials Science 163 (2019) 218-229.

Combined molecular dynamics and phase-field simulation investigations of crystal-melt interfacial properties and dendritic solidification of highly undercooled titanium

Sepideh Kavousi[1], Brian R. Novak[1], Mohsen Asle Zaeem[2], and Dorel Moldovan[1,3,*]

[1]*Department of Mechanical and Industrial Engineering, Louisiana State University, Baton Rouge, LA 70803, United States*

[2]*Department of Mechanical Engineering, Colorado School of Mines, Golden, CO 80401, United States*

[3]*Center for Computation and Technology, Louisiana State University, Baton Rouge, LA 70803, United States*

Abstract

The effects of kinetic and capillary anisotropies on crystal morphology and growth rate during solidification of titanium are studied using atomistically-informed phase-field simulations. Molecular dynamics (MD) is employed to calculate the anisotropic kinetic coefficient and crystal-melt interface free energy using the free solidification and capillary methods. The phase-field simulation results for solidification velocity and interface temperature are in quantitative good agreement with experimental and analytical data for undercoolings below 150K. As the role of interface kinetic effects increases with undercooling the use of a modified phase-field model allowed the extension of its quantitative prediction capability to higher undercoolings. In addition, the effect of MD calculated kinetic and capillary anisotropy parameters on dendrite shape and tip and solidification velocity was investigated.

KEYWORDS: titanium crystal-melt interfacial properties, molecular dynamics simulation, phase-field, dendritic solidification, highly undercooled melt

*Corresponding author: phone: 225-578-6488; e-mail: dmoldo1@lsu.edu

1. Introduction

Titanium and its alloys have unique properties and are among the most important metals for use as structural materials and are found in applications across many industries [1, 2]. Favorable properties such as mechanical strength, low density, and corrosion resistance makes titanium a preferred material in diverse areas such as aerospace [3], marine [4], and chemical industries [5]. Moreover, due to the excellent biocompatibility with human body, titanium and its alloys are the materials of choice for many medical applications, including bone and dental implants [6]. Given that the cost of titanium is relative high compared to other metals such as steel and aluminum there is great interest in further developments of cost effective parts and component fabrication approaches. As such, casting of titanium and titanium alloy parts offers unique cost savings over other metallurgical processing techniques as well as technological advantages by allowing the production of components with complex shapes and geometries. To a large extent the quality and integrity of the cast ingots is determined by their microstructural characteristics such as solute micro segregation, grain size and shape, porosity, etc., characteristics which develop during the dendritic solidification process. Therefore, the development of a better understanding of both material and technological casting parameters on the solidification process is of central importance and a great deal of progress in this direction, in addition to experimentation, is obtained by accurate modeling and simulation of dendritic solidification process [7]. In spite of the great progress in understanding dendritic solidification important issues remain unsolved, such as the quantitative prediction of crystal growth in highly undercooled liquid metals. Solidification is a free boundary problem that poses expensive computational challenges and various simulation methodologies have been used over the last decades, including phase-field method [7].

Phase-field modeling is a powerful and widely used simulation methodology for investigation of pattern formation. It was first introduced in the 1980's to study phase transition [8, 9] and was later expanded and applied to investigations in a multitude of areas such as solid state phase transformations [10, 11], crack nucleation and propagation [12], dislocation dynamics, and precipitation growth [13-16]. The early applications of phase-field modeling provided mainly a qualitative description of the solidification process. Subsequent improved geometrical models together with the incorporation of realistic crystal-melt interfacial free energy and/or kinetic anisotropies allowed for a more quantitative description and lead to the development of a variety of phase-field models used to study solidification of pure materials [13, 14, 17-23]. The thin

interface asymptotic analysis of the phase-field equations developed by Karma and Rappel relates the phase-field parameters to the free boundary solidification equations [24]. The interfacial free energy, kinetic coefficient, and their anisotropy coefficients are important input parameters and need to be known accurately for quantitative prediction in a phase-field simulation of solidification. Many studies show the importance of the effect of crystalline anisotropy on dendrite shape [25] and growth rate [26]. A major limiting factor of quantitative prediction of the characteristics of solidification process with phase-field simulation approach is the scarcity of available experimental data pertaining to crystal-melt interfacial properties, especially the anisotropy coefficients for interfacial free energy and kinetic coefficients of the materials. Because the undercooled melt solidifies very rapidly, there are only a few experiments that have successfully measured the solidification velocity, crystal-melt interfacial free energy and kinetic coefficient for large undercooling [27-29] and there are no reports on experimental measurement of interfacial anisotropy coefficients.

In the quest for obtaining accurate description of anisotropic energies and mobilities of crystal-melt interfaces computer simulations have become an increasingly important tool with MD simulations well positioned as the main method of choice. Calculations of kinetic coefficient using MD simulations was reported for various pure elements such as nickel [30, 31], gold and silver [32], aluminum [31], magnesium [33], and copper [31, 34], and also compounds such as Ni_3Al [35]. Moreover, the interfacial free energy and anisotropy coefficients was also obtained from MD simulations for aluminum [36], iron [37], magnesium [33], and gold and silver [38] elements, as well as alloys such as nickel-aluminum [39] and nickel-copper [40]. There is very limited data on crystal-melt interfacial properties of titanium. Specifically, the interfacial free energy [41, 42] and solidification velocity [43, 44] have been measured experimentally for titanium but the reported results show a large scatter and provide no information on anisotropies of these properties.

In this study, we focus on investigating the effects of kinetic and capillary anisotropies on the crystal morphology and growth rate in solidification of titanium using a combined MD with phase-field simulation approach. First, we report our calculations of the interfacial free energy, kinetic coefficient, and their anisotropies using MD simulations. Then using the MD calculated parameters in phase-

field simulations, together with other experimentally obtained properties of titanium, we investigate dendritic solidification of undercooled titanium. The phase-field solidification

velocities show good agreement with the experiment results for small undercooling but exhibits some deviations from the experiments for large undercoolings. By adopting and implementing a variant of phase equations, as proposed by Bragard et al [45], the agreement between simulation and experimental results is extended to higher undercoolings. Our study of the effect of the anisotropy parameters on the dendrite tip velocity and the overall solidification velocity also shows that the tip velocity is affected significantly while the effect on the overall velocity is much smaller.

2. Simulation Methodology

The solidification of a pure melt is governed by the heat diffusion equation in the solid and liquid with a temperature boundary condition imposed on crystal-melt interface. In addition to heat diffusion equation, the boundary condition should also include the crystal-melt boundary heat source term, in the form of the Stefan condition, that relates the solidification velocity to the jump in normal temperature gradient at the interface. The temperature at any point along the moving crystal-melt interface, T_I, is governed by the velocity-dependent Gibbs-Thomson (GT) relation [7] given by:

$$T_I = T_M - \frac{T_M}{L}\sum_{i=1,2}\frac{1}{R_i}\left[\gamma(\hat{n}) + \frac{\partial^2\gamma(\hat{n})}{\partial\theta_i^2}\right] - \frac{V_{\hat{n}}}{\mu(\hat{n})}, \quad (1)$$

where T_M is the melting temperature and L is the latent heat of melting per unit volume. The second term on the right-hand side of Eq. (1) represents the local change of the interface equilibrium temperature due to the curvature of the interface, where R_i (i=1,2) are the local principal radii of curvature, $\gamma(\hat{n})$ is the interfacial free energy, $\gamma(\hat{n}) + \frac{\partial^2\gamma(\hat{n})}{\partial\theta_i^2}$ is the interfacial stiffness, and θ_i are the local angles between the interface normal direction ($\hat{n}$) and the two local principal directions. The last term on the right-hand-side of Eq. (1) represents the non-equilibrium interface undercooling that drives the solidification, where $\mu(\hat{n})$ and $V_{\hat{n}}$ are the kinetic coefficient and solidification velocity for the interface normal direction, respectively. It is therefore crucial to determine both the magnitude and anisotropy of interfacial free energy and kinetic coefficient.

2.1 Selection of interatomic potential for MD simulations

When calculating crystal-melt interfacial properties by MD simulations it is very important to identify and use the best available inter-atomic potential for the system of interest at the appropriate external conditions, in this case titanium close to melting temperature. Accordingly, we considered

four existing interatomic potentials for Ti; three of the modified embedded atom method (MEAM) potential type (MEAM bcc [46], MEAM hcp [47], MEAM spline [48]) and one embedded atom method (EAM) potential (EAM [49]). In the evaluation process of the four inter-atomic potentials, we factored in the capability of the potentials to accurately reproduce important properties of titanium: the high temperature crystal structure, the radial distribution function $g(r)$ of the liquid phase, the melting temperature, the latent heat of fusion, and the diffusivity in the liquid phase.

Table 1: *The melting temperature, latent heat of fusion, and liquid diffusivity at the melting point as obtained from MD simulations of titanium by using four interatomic interaction potentials and from experimental data. Unless specified otherwise, the melting temperatures and latent heats are from the references indicated. The diffusivities for all four potentials were obtained from our MD calculations*

Interatomic potential and crystal structure	Melting temperature [K]	Latent heat [kJ/mol]	Liquid diffusivity [$\times 10^{-5}$ cm^2/s]
EAM, hcp [49]	1918	12.5	4.7*
MEAM, bcc [46]	1651; 1716*	11.7; 9.07*	5.7*
MEAM, hcp [47]	1706	14.5	3.9*
MEAM spline, bcc [48]	1900; 1876*	9.09*	3.9*
Experiment [50]	1941	14.17	4.9

* Result obtained from our MD simulations using the corresponding interatomic potential

Table 1 presents a summary of the MD simulation results for the melting temperature, the latent heat of fusion, and the liquid diffusivity at the melting temperature for titanium modeled by each of the four interatomic potentials considered and the corresponding data from experimental measurements. The latent heat of fusion and the melting temperature for the MEAM bcc and MEAM spline bcc potentials were calculated by the method presented in [51] and the values obtained were slightly different than the values reported in [46] and [48]. The values for the same thermodynamic properties reported for the EAM hcp and MEAM hcp potentials are closer to the experimental data. The diffusivities in the liquid phase are relatively close to the experimental value for all four potentials. In addition to their ability at predicting thermodynamic and transport

properties, the four interatomic potentials were evaluated on their potential at reproducing crystal structure and structural characteristics of the liquid phase. Figure 1 shows the MD-calculated pair distribution functions, $g(r)$, the experimentally obtained g(r) at 1,965 K [52], and the pair distribution function obtained by *ab initio* MD simulation at 2,000 K [53, 54]. Although the EAM hcp potential predicts the melting point and latent heat of fusion close to experimental values, the g(r) shows significant deviation from the experimental and ab-initio g(r) functions, especially close to the second and third extrema. Titanium has a stable hcp crystal structure at room temperature and, as temperature rises above 1,150 K, it undergoes an allotropic structural transformation to a bcc crystal structure. The MEAM hcp potential was rejected because it does not have a stable bcc phase. The latent heats for the MEAM bcc and MEAM spline bcc potentials are similar, but the $g(r)$ and liquid diffusivities for the MEAM bcc potential are closer to experimental and *ab initio* MD simulation data and therefore we settled on the MEAM bcc potential [46] as the inter-atomic potential for our MD simulations of Ti. All MD simulations were performed using the LAMMPS software [55].

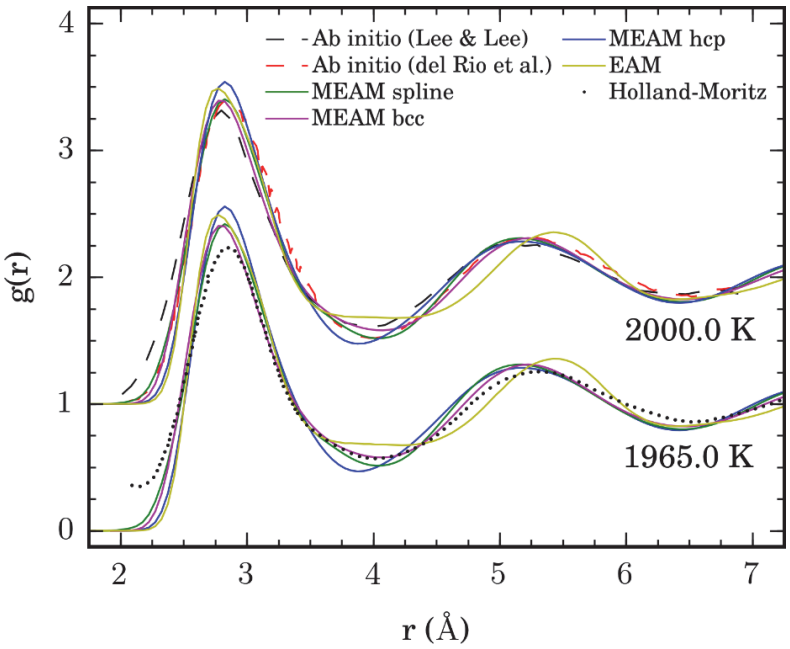

Figure 1 : *Comparison of radial distribution functions for pure titanium obtained from classical MD simulations with MEAM spline [48], MEAM bcc[46], MEAM hcp [47], EAM potential [49], ab initio MD simulations [53, 54], and Holland-Moritz experimental data [52].*

2.2 Calculation of kinetic coefficient

The MD simulation approaches used for calculation of the kinetic coefficient of crystal-melt interfaces can be divided into equilibrium and non-equilibrium methodologies [7]. The equilibrium methods rely on the analysis of the fluctuations of the crystal-melt interface through the capillary fluctuation method [7]. The non-equilibrium MD methods are classified as either forced velocity [56, 57] or free solidification [57] approaches. In this study the kinetic coefficient was calculated by using a free solidification method [57]. Under the MD simulation conditions, the crystal-melt interface, on average, remains planar during the solidification and therefore according to Gibbs-Thomson relation (see Eq. (1)) the slope of the solidification velocity as function of temperature gives the kinetic coefficient. Due to the latent heat generated during solidification, the interface region will be at a higher temperature if only a single global thermostat is used. To eliminate the temperature gradients and avoid the calculation of interface temperature we used a system of multiple local thermostats applied independently to thin slabs aligned parallel to the plane of the solidification interface. This approach was proven to provide nearly identical results to those obtained by using a global thermostat and the actual interface temperature calculation [57].

Calculation of the kinetic coefficient requires determination of the velocity of the crystal-melt interface at different undercoolings, but initially an equilibrated crystal-melt coexistence system at the melting temperature of 1716 K is needed. For a (001) oriented solidification interface, shown in Figure 2, the whole simulation system was initialized on a lattice consisting of 14×14×69 bcc unit cells (27,048 atoms) of approximate dimensions 46×46×230 Å. The simulation systems with different orientations of the crystal-melt interface, (110) and (111), have similar dimensions and number of atoms. Next, the system was equilibrated for 50 ps as a solid under the NPT ensemble where P = 0, followed by an additional 300 ps simulation during which the mean lattice parameter was determined. To create the crystal-liquid coexistence system, the central three quarters portion of the simulation box along the z-direction (see Figure 2) was melted by heating it at 2,600 K for about 50 ps under the NVT ensemble while the other quarter of the system remained in the original (solid) state. This lead to the creation of two crystal-melt interfaces. Finally, the equilibrated crystal-melt coexistence system was obtained by a 100 ps MD simulation under $NP_{zz}T$ conditions in which the temperature of the entire system is set to the melting temperature and the normal stress in the z direction, P_{zz}, is zero. The box sizes in the x and y directions, after they were adjusted to the values determined by the average lattice parameter for the melting temperature, were

maintained fixed. An additional 100 ps NPT simulation was used to obtain the equilibrated crystal-melt coexistence configurations that were used as the starting configurations for non-equilibrium solidification.

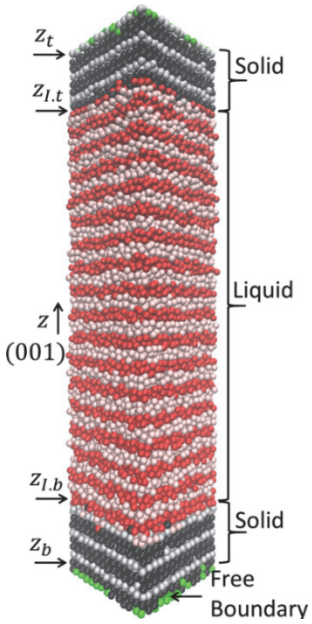

Figure 2: *The starting configuration of the system used for the nonequilibrium MD simulations of solidification of pure titanium. Red/pink and dark gray/light gray regions are located in liquid and solid phases respectively. Alternating dark/light colors are used to clearly indicate the adjacent slabs that are thermostated independently. The green atoms are boundary atoms which were restrained to have an average force of zero in the x and y directions.*

Starting from the equilibrated crystal-melt coexistence system, the kinetic coefficient is calculated from the investigation of the variation of the crystal-melt interface velocity with the applied undercooling. For these, the values of the lattice parameter for various undercooling temperatures were needed. These were obtained from a set of separate MD simulations of the solid at the corresponding temperatures similar to those performed at the melting point but with a smaller box size of only 13×13×13 unit cells (4394 atoms). Starting from an equilibrated crystal-melt coexistence configuration, the velocities of all atoms are scaled down to obtain the desired temperature below the melting point. |The boundary conditions in the z-direction are changed from periodic to free boundaries, the barostat is turned off, and the box sizes and atom positions are scaled in the x- and y-directions (the interface plane) such that the solid regions have the lattice

parameter appropriate for the undercooled temperature. The solidification step is effectively run under conditions of constant normal stress due to the free boundaries (P_{zz} = 0) and constant temperature where the undercooled temperature is maintained by using the multiple thermostats approach in which the simulation system is divided along the z direction into a set of slab regions parallel to the interface and each slab is independently thermostatted. The free boundaries along the z-direction are required in order to be able to use multiple regional thermostats. Surface melting was observed at the free boundaries, especially for small undercoolings. To prevent surface melting, the atoms located in the two atomic planes adjacent to the free boundaries were restrained such that the average forces in the x and y directions on those groups of atoms were set to zero and the temperature in these regions was maintained to the desired undercooling by applying a Langevin thermostat with a damping parameter of 0.1 ps only in the z direction. The thickness of all of the other regional thermostats was set to 5.0 Å and velocity rescaling was used whenever the temperature deviated more than 1 K from the target temperature. Ten independent solidification simulations were run starting from different initial coexistence configurations to determine the uncertainty in interface velocity for each undercooling.

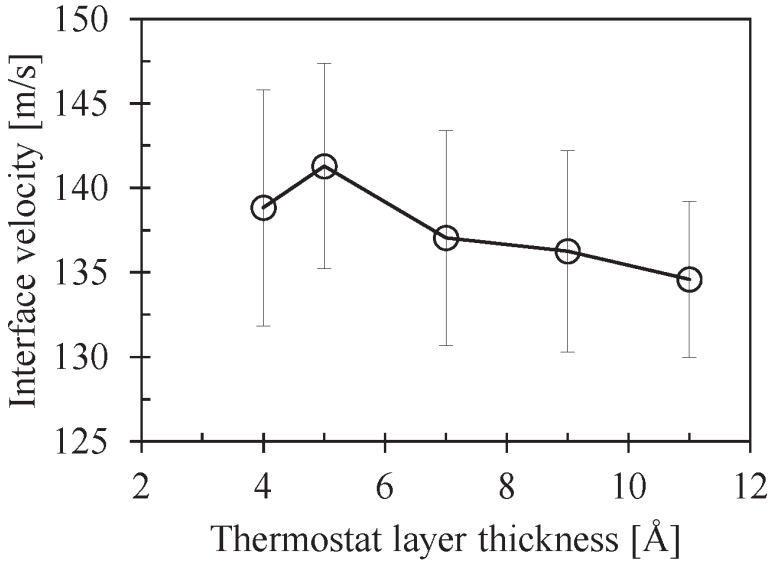

Figure 3*: Crystal-melt interface velocity as a function of thermostat bin thickness with 200 K undercooling. Error bars represent 95% confidence intervals.*

The selection of the optimum thermostats bin thickness was based on the analysis of the variation of crystal-melt interfacial velocity with the bin thickness for a given temperature

undercooling. Figure 3 shows that the decrease of bin thickness leads to an increase of interface velocity and for a 200K undercooling it reaches a plateau for bin thickness less than 5 Å.

The velocity of the interface was calculated by using two methodologies. The so-called indirect method relies on the relationship between interface velocity and the average slope of the variation of the total potential energy with time during a steady state solidification simulation at a given undercooling temperature T and is given by

$$v_{int} = \frac{1}{2AL}\frac{dE}{dt}, \tag{2}$$

where v_{int} is the interface velocity, A is the area of the interface, E is the total interatomic potential energy of the system. L is latent heat per volume of solid, $\langle V_{sol} \rangle$, and can be calculated as:

$$L = \frac{\langle H_{liq} \rangle - \langle H_{sol} \rangle}{\langle V_{sol} \rangle}, \tag{3}$$

where $\langle H_{sol} \rangle$ and $\langle H_{liq} \rangle$ are the enthalpies of solid and liquid respectively at the simulation undercooling temperature. The interface velocity is also obtained by direct tracking of the interface position as function of time and using

$$v_{int} = \frac{1}{2}\left[\frac{d(d_I)}{dt} - \frac{d(d_{Sys})}{dt}\right], \tag{4}$$

$d_I = z_{I,t} - z_{I,b}$ and $d_{Sys} = z_t - z_b$, where $z_{I,t}$ and $z_{I,b}$ are the positions of the top and bottom interfaces and z_t and z_b are the positions of the upper and lower solid layers, see Figure 4. Note that z_t and z_b change due to the volume change of solidification which must be accounted for when calculating the interface velocity. The time to reach steady state solidification is taken as the time to create solid with a 12 Å depth or about 3 layers at each interface which is sufficient so that the calculated velocity is no longer dependent on starting time.

Obtaining $z_{I,t}$ and $z_{I,b}$ requires use of an order parameter whose average value is clearly different in the liquid and solid phases. For convenience we use the centrosymmetry parameter, CS, based on 12 nearest neighbors, which is calculated for each atom in the system [58]. Twelve nearest neighbors is close to the number in the liquid phase and gave a larger difference between liquid and solid than the 8 nearest neighbors typically used for the bcc crystal. Although the centrosymmetry parameter fluctuates, the mean values in the liquid and solid phases are clearly

different as shown in Figure 4. To obtain the interface positions, the fitting of error function to CS is used:

$$CS_{fit} = \begin{cases} 0.5\left(\langle CS_{sol}\rangle + \langle CS_{liq}\rangle + \left(\langle CS_{sol}\rangle - \langle CS_{liq}\rangle\right) erf\left[\frac{z-z_{I,t}}{\sigma\sqrt{2}}\right]\right), & z_{center} < z < z_{upper} \\ 0.5\left(\langle CS_{sol}\rangle + \langle CS_{liq}\rangle - \left(\langle CS_{sol}\rangle - \langle CS_{liq}\rangle\right) erf\left[\frac{z-z_{I,b}}{\sigma\sqrt{2}}\right]\right), & z_{lower} < z < z_{center} \end{cases}, \quad (5)$$

$$z_{center} = 0.5(z_t - z_b) + z_b, \quad (6)$$

$$z_{upper} = 0.95(z_t - z_b) + z_b, \quad (7)$$

$$z_{lower} = 0.05(z_t - z_b) + z_b. \quad (8)$$

Although $\langle CS_{sol}\rangle$ and $\langle CS_{liq}\rangle$ can be obtained from averages by separate bulk solid and liquid simulations, we consider them to be adjustable parameters along with $z_{I,t}$, $z_{I,b}$, and σ. The fitting is performed using the *lmfit* python package [59] during the simulation at 0.375 ps intervals by utilizing the ability of LAMMPS [55] to use python functions. This feature also allows the simulations to be terminated when the distance between interfaces is less than 50 Å.

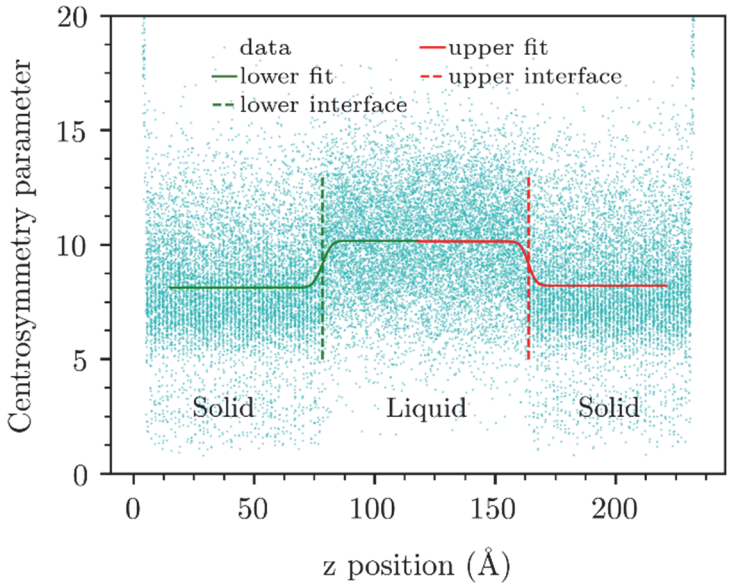

Figure 4: *Variation of the centrosymmetry parameter along the z direction (the solidification direction) at a given time during a MD simulation of the solidification in a crystal- melt coexisting system. The solid green and red lines depict the error function fit of the order parameter around the lower and upper interface respectively. The dashed green and vertical lines indicate the current location of the two crystal melt interfaces.*

2.3 Calculation of interfacial free energy and stiffness

There are various MD methods used to calculate the crystal-melt interfacial free energy such as the cleavage method [60], the critical nucleus method [61], metadynamics [62], transition interface sampling [63], the mold integration method [64], the interface pinning method [65], and the capillary fluctuation method [66]. Here, we use the capillary fluctuation method which was chosen due to its relative simplicity, ability to obtain anisotropy coefficients, and applicability to alloys for future use.

In the capillary fluctuation method, the MD simulation is performed at the melting temperature with crystal-melt coexistence. The system is quasi-two dimensional; the interface length (W) in the x direction is much larger than its width (b) in the y direction. The system is very long (L) in the interface normal direction to avoid any interactions between interfaces. The simulation system is shown in Figure 5.

Let $h(x)$ be the position along the z direction of an interface separating solid and liquid phases. Its deviation from the mean value, $\langle h \rangle$, can be written as a summation of Fourier modes: $h(x) - \langle h \rangle = \sum_k A(k)\, e^{ikx}$. Based on the equipartition of energy on the degrees of freedom applied to individual capillary fluctuation modes, the interface stiffness can be calculated using:

$$\gamma + d^2\gamma/d\,\theta^2 = \frac{k_B T}{bW\langle |A(k)|^2 \rangle k^2}, \tag{9}$$

where, $k_B T$ is the thermal energy, $\langle |A(k)|^2 \rangle$ is the mean squared amplitude of the Fourier modes and k is the mode wave number. The crystal-melt interface can also be considered two dimensional so instead of one stiffness, two different stiffness values must be considered in equation (9) [67]. Plotting $k_B T/(bW\langle |A(k)|^2 \rangle)$ versus k^2 and fitting for small values of k gives a slope which is the interface stiffness. The same procedure is repeated for different crystallographic orientations to obtain interface stiffness anisotropy coefficients.

The MD simulation starting configuration consists of a periodic system with dimensions of 80×4×220 bcc unit cells. The central half of the system is melted in the NVT ensemble at 2,600 K, while the remaining half of the atoms are fixed. The resulting crystal-melt coexistence system is equilibrated at the melting point for 1 ns in the $NP_{zz}T$ ensemble, using an extended system thermostat and barostat. Assuming the melting point is accurate, one can infer that the system is now close to equilibrium. The positions of the two crystal-melt interfaces are then obtained from

an NPH simulation lasting for 240 ps. During this step, the system configuration is saved every 0.2 ps for later analysis of the interface fluctuations.

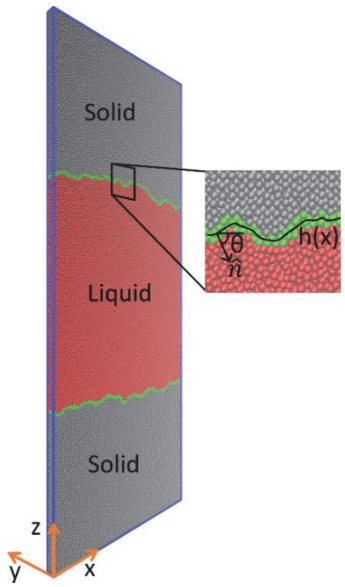

***Figure 5**: A snapshot from the MD simulation of pure titanium depicting the thermal fluctuations of the crystal-melt interface. The phase of each atom is based on the value of the atomic order parameter ψ defined in Equation (11). The gray atoms represent the solid and the red atoms represent the liquid phase. The green atoms are those located at the crystal-melt interface and the solid line represents the interface location where the order parameter has a value halfway between that of bulk solid and bulk liquid.*

To obtain the interface positions, $h(x)$ (see Figure 5), an order parameter is needed to allow us to distinguish the solid from the liquid. In the case of the kinetic coefficient calculations, only the average interface position was needed and therefore the choice of order parameter was not so critical. However, for the calculation of the interfacial free energy in addition to the average interface position one also needs to know the local interface position and, as such, the order parameter must be chosen more carefully. In this study we used the order parameter introduced by Sun et al. [30]. To start, for each atom, j, the order parameter, β_j, is calculated from the difference of the vectors to the 1NN and 2NN atoms, $\vec{r_i}$, to those same vectors in a perfect bcc crystal, $\overrightarrow{r_{bcc}}$, and normalized by the number of 1NN and 2NN neighbors and the lattice parameter squared, a^2.

$$\beta_j = \frac{1}{14a^2}\sum_i |\vec{r_i} - \overrightarrow{r_{bcc}}|^2. \quad (10)$$

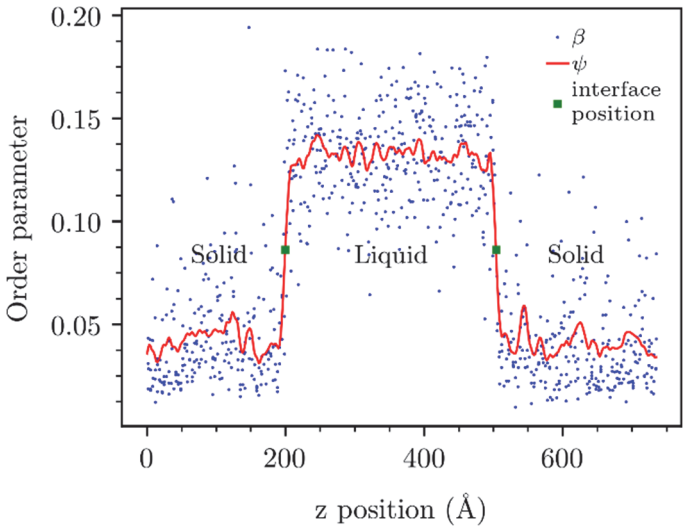

Figure 6: *The local order parameter, ψ, as a function of z for the* (001) *oriented interface for one value of x and β for atoms within 0.25a of that value of x.*

The values of this order parameter still exhibit large fluctuations which makes the determination of interface position difficult. To solve this issue, the smoothed order parameter, introduced by Asadi et al. [37], was used in this work:

$$\psi(x,z) = \frac{\sum_i w_d r_i \beta_i}{\sum_i w_d r_i}, \quad (11)$$

where $w_d = [1-(r_i/d)^2]^2$, $r_i = \sqrt{(x_i - x)^2 + (z_i - z)^2}$ and d is a smoothing distance. Large smoothing distances lead to inaccurate results and small smoothing distances do not sufficiently dampen the fluctuations. Note that ψ is obtained from a smoothing over cylinders perpendicular to the y direction, so it does not need to be calculated for each atom, only on a grid in the $x-z$ plane. We use a grid spacing of $0.5a$ and a smoothing distance of $d = 2.5a$, where a is the lattice parameter. Figure 6 shows ψ for one value of x and β for atoms within $0.25a$ of the same value of x along the z direction. The average values of ψ in the solid and liquid phases are estimated to be 0.038 and 0.135 respectively. The interface location is taken to be where ψ is halfway between those values, 0.086. Figure 6 shows that the interface positions can be easily determined using the ψ order parameter.

Once h(x) for each interface was calculated, the Fourier transform was applied and amplitude of each Fourier mode was determined. The amplitudes of the Fourier modes for all times were then squared and averaged to obtain $\langle|A(k)|^2\rangle$. The slope of $k_BT/(bW\langle|A(k)|^2\rangle)$ versus k^2 for small k yields the stiffness value.

2.4 Phase-field model

2.4.1 Governing equations

The specific of the implementation of the phase-field model and the governing equations for solidification of pure materials are found in the book of Provatas and Elder [68]. In the following, only the important equations are provided and discussed.

The solidification of a pure material can be described by considering two field variables. One is the phase-field order parameter, ϕ (ϕ = 0 for liquid and ϕ = 1 for solid), and the other is the temperature, T. The evolution of the solidifying system is driven by the decrease of total free energy of the system which can be written in the form of the Ginzburg-Landau type free energy:

$$F = \int \left[\frac{\varepsilon(\hat{n})^2}{2}|\nabla\phi|^2 + f_{dw}(\phi, T)\right] dV \quad . \tag{12}$$

The first term is the excess free energy due to the interface and the second term is the bulk free energy density. Phase-field simulation methodologies allow for significant freedom when choosing the functional form for bulk free energy term. In this study, we consider the form of $f_{dw}(\phi, T)$ as follows:

$$f_{dw}(\phi, T) = wg(\phi) + h(\phi)\frac{L_0}{T_m}(T - T_m) \, , \tag{13}$$

where $g(\phi) = \phi^2(1-\phi)^2$ represents the double-well Ginzburg-Landau free energy function, $wg(\phi)$ is the free energy distribution, and $h(\phi) = \phi^3(10 - 15\phi + 6\phi^2)$ is the so-called smoothing function with 0 and 1 values in the liquid and solid phases, respectively [45]. The time evolution of the order parameter is described by the phase-field equation:

$$\frac{\partial\phi}{\partial t} = -M\frac{\delta F}{\delta\phi} \, , \tag{14}$$

where M is the mobility related to the kinetic coefficient as described below. After taking the functional derivative in (14) and by considering the time evolution of the thermal diffusion field subject to the crystal-melt interface conditions, the final time-evolution equations [69] for the two field variables, T and ϕ, are:

$$\frac{\partial T}{\partial t} = D\nabla^2 T + \frac{L_0}{c_p} h'(\phi) \frac{\partial \phi}{\partial t}, \tag{15}$$

$$\frac{1}{M(\theta)} \frac{\partial \phi}{\partial t} = \nabla . (\varepsilon(\theta)^2 \nabla \phi) + \frac{\partial \left(\varepsilon(\theta) \varepsilon'(\theta) \frac{\partial \phi}{\partial x} \right)}{\partial y} - \frac{\partial \left(\varepsilon(\theta) \varepsilon'(\theta) \frac{\partial \phi}{\partial y} \right)}{\partial x} - w g'(\phi)$$

$$- h'(\phi) \frac{L_0}{T_m} (T - T_m) + Noise(\phi). \tag{16}$$

Both ϕ and T are functions of position, r, and time, t. For most crystalline materials, especially metals, both the crystal-melt interfacial free energy and the kinetic coefficient depend on the orientation of the crystal-melt interface. Typically, in a phase-field model the anisotropy effect is accounted for by considering the dependence of the ε and M parameters on the angle, θ, between the direction normal to the interface and a specified direction in crystal.

The side branching of dendrites arises from thermal fluctuations. To mimic the thermal fluctuations in a phase-field model, a continuous source of noise is added to the right hand side of Eq. (16):

$$Noise(\phi) = 16R\phi^2(1-\phi)^2, \tag{17}$$

where R is a randomly generated number that takes values between -1 and +1.

The system of governing equations (Eqs. (15), and (16)) for the evolution of the phase-field order parameter and temperature are solved numerically using a finite difference algorithm. All terms on the right-hand side of Eq. (16), except the Laplacian term, are discretized using a second order scheme, and for the Laplacian term we used the fourth order skewed 9-point scheme. The simulations are carried out on a 400 × 400 grid with $\Delta x = \Delta y = 0.5\zeta_p$ and $\Delta t = 10$ ps where ζ_p is the interface thickness which was set to be larger than the microscopic capillary length.

2.4.2 Relationship between phase-field and thin-interface models

The present work focuses on a two-dimensional (2D) implementation of a phase-field model for investigation of solidification in undercooled titanium. Thin interface analysis was used to map the phase-field equations to the classical sharp-interface moving boundary equations for solidification; the mapping is applicable in the limit where the interface thickness is small compared to the characteristics length-scales of the microstructure which is the case for metals. Using this method, the ε_0, w, and M parameters present in the phase-field equations are calculated

by using the MD calculated crystal-melt interfacial free energy and its kinetic coefficient by using the following equations:

$$\zeta_p = \frac{\varepsilon_0}{\sqrt{w}} 2\sqrt{2}\, ln3, \tag{18}$$

$$\gamma = \frac{\varepsilon\sqrt{w}}{3\sqrt{2}}, \tag{19}$$

$$\frac{1}{\mu} = \frac{1}{3\sqrt{2}} \frac{T_m\sqrt{w}}{\varepsilon L_0 M} - \frac{L_0}{D c_p} \frac{\varepsilon}{\sqrt{2w}} \int_0^1 \frac{h(\phi)(1-h(\phi))}{\sqrt{g(\phi)}}\, d\phi \tag{20}$$

The asymptotic analysis to construct the mapping of the parameters as given in Eqs. (18), (19), and (20) is rather complicated and can be found in [24]. All of the other thermophysical properties and phase-field parameters for titanium are listed in Table 4 in Section 3.3.

3 Results and Discussion

3.1 Kinetic coefficient

Figure 7 shows the MD simulation results for interface velocity versus undercooling temperature for different interface orientations where the interface velocity was obtained using both direct (Eq. 4) and indirect (Eq. 2) methods. Due to the periodic boundary conditions, the interface is planar on average. Therefore, based on the Gibbs-Thomson equation, we expect a linear relationship between interface velocity and undercooling temperature. The kinetic coefficient is given by the slope of the velocity-undercooling curve.

For a crystal with cubic symmetry, the kinetic coefficient as a function of interface orientation is given by:

$$\frac{1}{\mu(\hat{n})} = \frac{1}{\mu_0}(1 + 3\varepsilon_k - 4\varepsilon_k \textstyle\sum_{i=1}^{3} n_i^4) \quad , \tag{21}$$

where n_i are the components of the unit vector, $\hat{n}$, normal to the interface plane, μ_0 is the average kinetic coefficient, and ε_k is the anisotropy parameter [66].

Table 2 summarizes the information about the orientations, the kinetic coefficient expressions as given by Eq. (21), and the calculated values from MD simulations. $< >$ denotes the interface in-plane crystallographic orientation in the x direction and { } denotes the orientation characterized by the normal to the crystallographic plane parallel to the interface. For crystals with cubic symmetry, only the crystal orientation in the interface normal direction should affect the kinetic coefficient. The MD results proved that this is indeed true as evident from the results obtained for

$\langle 1\bar{1}0\rangle\{110\}$ and $\langle 001\rangle\{110\}$ orientations for which the kinetic coefficient differ by only about 1%. Direct and indirect calculation of interface velocity gives approximately the same results, but the indirect method gives consistently lower kinetic coefficients.

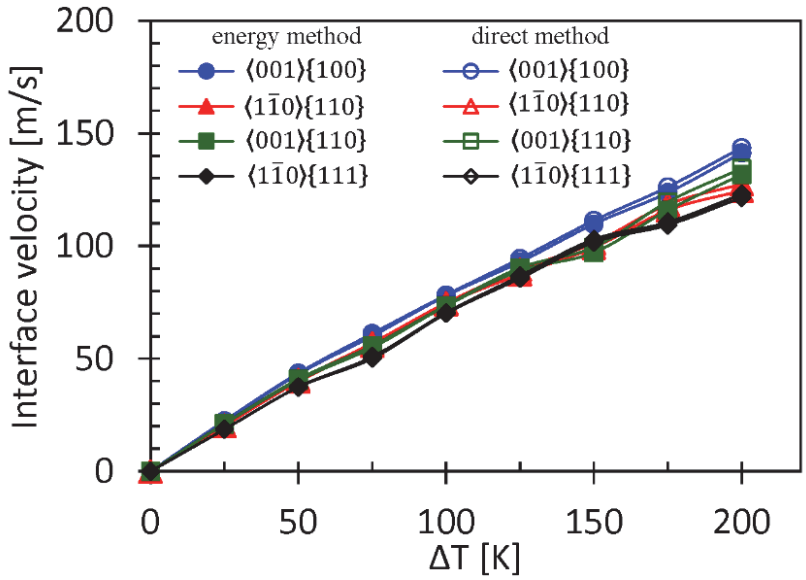

Figure 7: *The interface velocity versus undercooling temperature from MD simulations of titanium obtained using two different methods. Four different interface orientations were considered. Uncertainties are comparable to the symbol sizes, so error bars are not shown. Uncertainties ranges from 3 to 13 % with lower velocities having larger percent uncertainty.*

Table 2: *The crystal melt interface kinetic coefficient for various interface orientations as given by Eq. (21) and MD simulations.*

Interface orientation	Kinetic coefficient [m/(s-K)]		
	Expression (Eq. 21)	Direct method	Indirect method
$\langle 001\rangle\{100\}$	$\mu_{001} = \mu_0/(1-\varepsilon_k)$	0.740 ± 0.030	0.729 ± 0.031
$\langle 1\bar{1}0\rangle\{110\}$	$\mu_{110} = \mu_0/(1+\varepsilon_k)$	0.684 ± 0.038	0.668 ± 0.039
$\langle 001\rangle\{110\}$	$\mu_{110} = \mu_0/(1+\varepsilon_k)$	0.691 ± 0.030	0.677 ± 0.033
$\langle 1\bar{1}0\rangle\{111\}$	$\mu_{111} = \mu_0/(1+1.667\varepsilon_k)$	0.654 ± 0.034	0.647 ± 0.034

Using the results from MD calculations and Eq. (21) one can calculate the mean kinetic coefficient and anisotropy. The direct method for obtaining interface velocities gives $\varepsilon_k = 0.037$ and $\mu_0 = 0.71$ m/(s-K) and the indirect method gives $\varepsilon_k = 0.04$ and $\mu_0 = 0.7$ m/(s-K). The values for the parameters μ_0 and ε_k were obtained without using the data for $\langle 1\bar{1}0 \rangle \{111\}$ orientation and therefore this can instead be used as a check. Specifically, the values of μ_{111}, obtained by using μ_0 and ε_k, are 0.669 m/(s-K) and 0.656 m/(s-K) for the direct and indirect methods, respectively. These values are reasonably close to the simulation values.

3.2 Interfacial free energy and stiffness

Figure 8 shows the variation of $k_B T/bW < |A(k)|^2 >$ versus k^2 for three different crystal-melt interface orientations in the x direction as obtained from MD simulations. The slope of the solid line is the stiffness value for that orientation. The data shows deviation from linearity for large values of k^2, and therefore there is a question of how much data at large k^2 value one should use for fitting. There is no precise way to decide on this issue, therefore in our procedure we keep adding points with higher k until the R^2 for the fit falls below 0.95 which is similar to [37] where the criterion used was the norm of the residuals being greater than 3. Eq. (22) suggests that the stiffness value is only a function of interface normal orientation. In MD simulations, two systems with $\{111\}$ orientations in interface normal direction are studied. In one of the systems the x direction was chosen to be $\langle 1\bar{1}0 \rangle$ and in the other it was $\langle 11\bar{2} \rangle$. In spite of choosing a quasi-2D system geometry with different crystallographic orientations for the x direction, the stiffness values are approximately equal. The same is true for the two simulation systems with $\{110\}$ orientations.

Similar to kinetic coefficient, for a crystal with cubic symmetry, the interfacial free energy as a function of orientation can be represented by the following equation:

$$\gamma = \gamma_0 \left[1 + \delta_1 \left(\sum_{i=1}^{3} n_i^4 - \frac{3}{5}\right) + \delta_2 (3 \sum_{i=1}^{3} n_i^4 + 66 n_1^2 n_2^2 n_3^2 - 17/7)\right] \qquad (22)$$

where γ_0 is the average interfacial free energy, δ_1 and δ_2 are the anisotropy parameters, and n_i is defined as in Eq. (21) [37]. Table 3 contains the calculated interface stiffness using the capillary fluctuation method. The parameters from Eq. (22) were obtained by a best fit to the MD data are

γ_0=176 mJ/m^2, δ_1=0.018, and δ_2=-0.0001. The MD calculated interface free energy is consistent with the reported experimental values ranging between 147 and 207 mJ/m^2 [42].

Table 3: *The crystal melt interface stiffness for various interface orientations as given by Eq. (22) and obtained from MD simulations.*

Interface orientation	Interface stiffness [mJ/m^2]	
	Expression (Eq. 22)	MD simulations
$\langle 100\rangle \{001\}$	$\gamma_0 [1- (18/5)\ \delta_1 - (80/7)\ \delta_2]$	156
$\langle 1\bar{1}0\rangle \{110\}$	$\gamma_0 [1+ (39/10)\ \delta_1 + (155/14)\ \delta_2]$	179
$\langle 001\rangle \{110\}$	$\gamma_0 [1- (21/10)\ \delta_1 + (365/14)\ \delta_2]$	177
$\langle 1\bar{1}0\rangle \{111\}$	$\gamma_0 [1+ (12/5)\ \delta_1 - (1280/63)\ \delta_2]$	193
$\langle 11\bar{2}\rangle \{111\}$	$\gamma_0 [1+ (12/5)\ \delta_1 - (1280/63)\ \delta_2]$	186

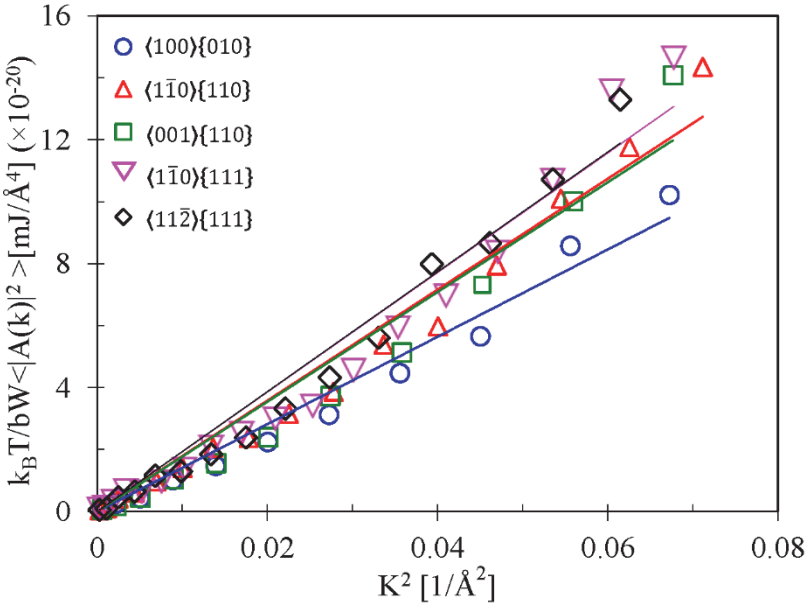

Figure 8: *The varition of $k_BT/bW<|A(k)|^2>$ versus k^2 for different orientations as obtained from MD simulation of titanium. The solid lines are linear fits where the color of the line is the same as the symbols for the data it was fit to.*

3.3 Phase-field simulation

The set of parameters entering the phase-field equations (Eqs. (15), and (16)) are summarized in Table 4. These parameters were obtained by either MD simulations combined with thin-interface to phase-field mapping, as explained previously, or were taken from existing experimental data [50]. In 2D, the anisotropic ε and M parameters can be obtained from Eqs. (23), and (24) in which θ is given by Eq. (25) where ϕ_x and ϕ_y are the derivatives of ϕ with respect to x and y respectively:

$$\varepsilon = \varepsilon_0(1 + \delta_\varepsilon \, cos(4\theta)) \tag{23}$$

$$\frac{1}{M} = \frac{1}{M_0}(1 - \delta_M \, cos(4\theta)) \tag{24}$$

$$\theta = tan^{-1}\left(\frac{\phi_y}{\phi_x}\right) \; . \tag{25}$$

Although the mobility anisotropy parameter, δ_M, depends on both μ and ϵ anisotropy parameters as shown in Eq. (20), it will be referred to as the kinetic anisotropy and δ_ϵ will be referred to as the capillary anisotropy.

Table 4: *Thermophysical properties and phase-field parameters for titanium. The parameters were obtained by either MD simulations or by combined MD with thin-interface to phase-field mapping or, for those properties indicated by *, were taken from existing experimental data [50].*

L_0 [kJ/mol]	14.3 *	D [m^2/s]	9.5×10^{-5} *
C_p [kJ/mol K]	45.5 *	T_m [K]	1943 *
ρ [kg/m^3]	4130 *	γ_0 [mJ/m^2]	176
w [J/m^3]	2.9×10^7	ζ_p [m]	8×10^{-8}
ε_0 [$\sqrt{J/m}$]	0.000138	M_0 [m^3/sJ]	6.76
δ_ε	0.00455	δ_M	0.021

Figure 9 shows the comparison of the steady-state solidification rate obtained from our phase-field simulations, two sets of experimental data [43, 44], and from the analytical Lipton-Kurz-Trivedi (LKT) model [70] parameterized for titanium. The results from the phase-field simulations, based on the model described by Equations (15), and (16), are in reasonable agreement with the results from both experiments and LKT model for undercooling, ΔT, below 200 K. When ΔT is larger than 200 K, the phase-field and experimental results start to deviate from each other and the deviation increases with increasing undercooling. The question is, what is the source of this discrepancy? Is it caused by the inaccuracies of experimental investigations, by the limitations and inaccuracies of the phase-field model or by both simulations and experiment? In the experiments, the solidification investigations at large undercoolings were done under electromagnetic levitation conditions. The nucleation of the solid phase was initiated by using a needle and establishing a contact with the levitating titanium droplet; the subsequent solidification time was estimated by tracking the evolution of the temperature at the top and bottom edge of the solidifying droplet. The solidification was considered to be completed when the temperature of the droplet top surface started to increase with respect to the undercooling temperature. As predicted by homogeneous nucleation theory, for undercooling in titanium smaller than 400 K, the probability of homogeneous nucleation in the liquid phase is very low, and therefore the nucleation process is unlikely to play any major role in determining the high solidification velocities obtained experimentally for large undercooling. It is therefore important to focus on possible sources of inaccuracies associated with model formulation, parameterization, and code implementation of phase-field simulation methodology.

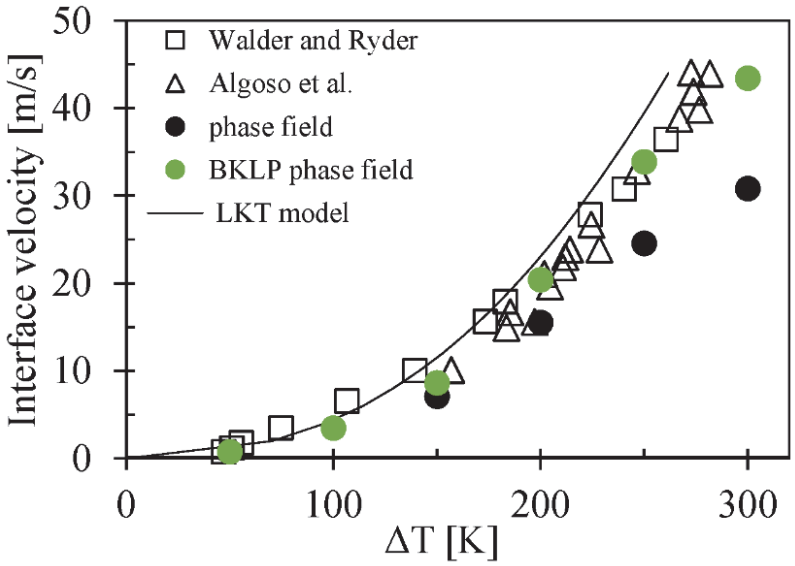

Figure 9: *Interface velocity versus undercooling in titanium as obtained from phase-field simulations, two sets of experiments (Walder and Ryder 1995, R. Algoso, S. Altgilbers et al. 2003), and from the LKT analytical model.*

As evident from Figure 9, the phase-field simulations indicate that the variation of the interface velocity with undercooling exhibits a crossover from linear to an approximately square root dependence when the undercooling is about 150 K. To gain additional insight into the role of the phase-field simulation model on the existence of such a crossover we performed additional phase-field simulations based on slightly modified models. First, we investigate the solidification in a system with one-dimensional (1D) symmetry. Specifically, the equivalent of equation (16) for the order parameter in one dimension and in a reference frame that is translating with velocity V_n along the +x direction can be written in the following form:

$$-\frac{V_n}{M}\frac{\partial \varphi}{\partial x} = \varepsilon^2 \frac{\partial^2 \varphi}{\partial x^2} - wg'(\phi) - h'(\phi)\frac{L_0}{T_m}\Delta T. \tag{26}$$

This can be rewritten in dimensionless form by normalizing the spatial and temperature variables $x' = \frac{x}{\bar{X}}$, $u = \frac{T}{L_0/c_p}$, where $\bar{X} = 10^{-6}\, m$. The dimensionless form of Eq. (26) in terms the new variables is:

$$-\frac{V_n}{\bar{X}}\frac{\partial \phi}{\partial x'} = \frac{\varepsilon^2}{\bar{X}^2}\frac{\partial^2 \phi}{\partial x^2} wg'(\phi) - h'(\phi)\frac{{L_0}^2}{c_p T_m}(u - u_m) \quad . \tag{27}$$

In the phase-field method, the order parameter increases monotonically from zero to one as a function of position in the interfacial region and remains constant far from the interface. For each undercooling, there is only one specific value of V_n, which results in a physically valid solution of Eq. (27); it complies with the desired order parameter shape explained above [45]. Solving this boundary value problem with one unknown parameter was done by using *bvp4c* solver in MATLAB [71]. The solution of this second order boundary value problem with one unknown parameter requires the knowledge of three boundary conditions. The order parameter values are zero and one at -∞ and ∞ respectively and the derivative of the order parameter far from the interface is zero in both liquid and solid phases.

By solving the Equation (27) for different values of ΔT, one can compute the interface velocity $V_n(\Delta T)$. Figure 10 shows the variation of the interface velocity with undercooling during solidification in a 1D system. Similar to the results obtained in phase simulations in the 2D system, discussed previously, for small undercoolings, up to ΔT ≈ 150 K, $V_n(\Delta T)$ varies approximately linearly with ΔT. At larger undercoolings, the interface velocity variation with undercooling follows a trend similar to 2D simulations at high undercoolings, and the undercooling temperature at which the deviation from linearity occurs is very close to undercooling temperature at which the 2D phase-field simulation results start to deviate from the experimental results as seen from Figure 9.

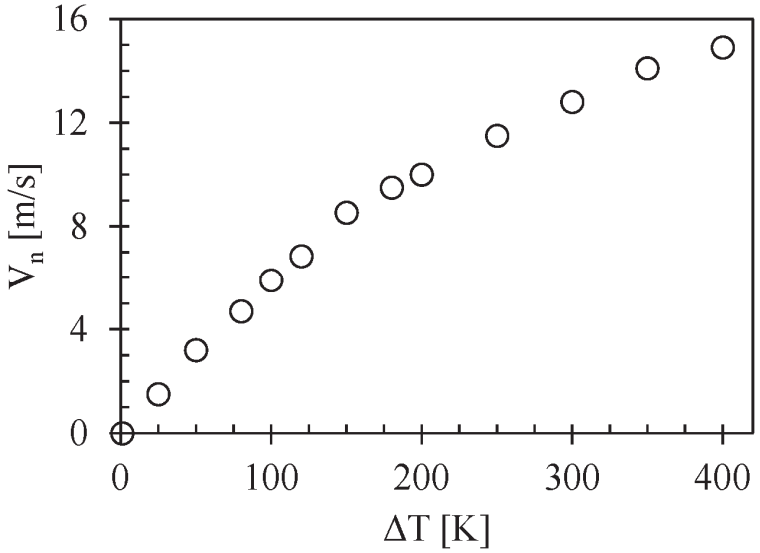

Figure 10: *Variation of the steady state velocity of a planar one-dimensional interface with undercooling.*

Based on the phase-field simulation results in both 2D and 1D systems one can infer that the deviation from linearity of the interface velocity versus undercooling at large undercoolings might be related to the actual phase-field model as represented in Equations (15) and (16). Building on the methodology developed by Bragard *et al*. [45] we implemented and used a modified phase-field model that seem to mitigate the shortcomings present at large undercooling in the regular phase-field model. The modification proposed by Bragard et al. consist of introduction of a new form of the driving force term in the bulk free energy density function (the second term in the right-hand side of Eq. 13) of the phase-field method. Specifically, in this method the relationship between thermodynamic driving force and undercooling is chosen to behave like $V_n^{-1}(\Delta T)$, which is the inverse of the function V_n. The simulation results, based on the Bragard et al. modifications, hereby referred to as the BKLP phase-field model, are also shown in Figure 9 and are in good agreement with the experimental results.

Another way that one can check the accuracy of phase-field simulation results is to compare the values of the interface temperature as obtained from simulation with those calculated by using the analytic Gibbs-Thomson (GT) relation in Equation (1). Based on the phase-field formulation, the crystal-melt interface is at local equilibrium and as such the interface temperature must follow the GT equation. According to GT relation, the deviation of the interface temperature from the melting point is due to both capillary and kinetic effects and can be calculated by knowing: the interface velocity, interface stiffness, dendrite tip curvature, and kinetic coefficient. Figure 11 shows the variation with undercooling of the interface temperature as obtained directly from the phase-field simulations and from the GT relation. The results from both phase-field and BKLP phase-field are presented. The calculation of the interface temperature from the GT relation is based on the following data: the MD calculated kinetic coefficient and stiffness, the phase-field calculated interface velocities (depends on the actual phase-field model used), and tip curvatures.

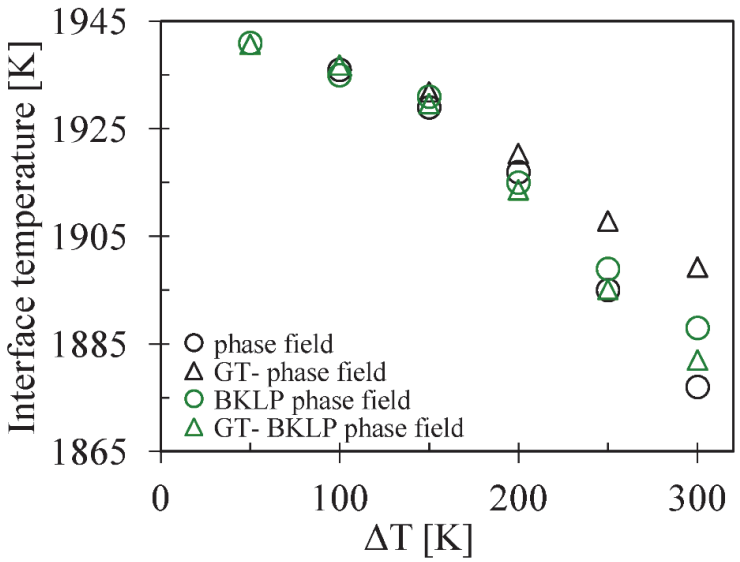

Figure 11: *The variation with undercooling of the interface temperature as obtained by direct temperature calculation from phase-field simulations and by use of Gibbs-Tompson equation.*

As evident from Figure 11, for small undercoolings, $\Delta T < 150$ K, there is a good agreement between the interface temperatures obtained directly from the phase-field model and GT relation; this is true for both phase-field models used. As the undercooling increases above 150K the deviation between the interface temperature calculated directly from phase-field simulation and the value calculated from GT equation increases for both phase-field models. It is however evident that when the BKLP phase-field is used, the direct and GT interface temperatures are close to each other even at high undercoolings; the difference is less than 10 K at $\Delta T = 300$ K. When the phase-field model based on Eq. (15) and (16) is used the difference between the GT temperature and the direct temperature from phase-field is about 32 K at $\Delta T = 300$ K. One can rationalize these differences by the following observations: For small undercooling, both the capillary and kinetic effects play a role in determining the interface temperature. Although the dendrite tip shape has a higher curvature for larger undercooling, the effect of the kinetic term is still more dominant than the capillary one due to the large solidification velocity. Therefore, underestimation of the velocity calculated from the phase-field method accounts for most of the deviation of the interface temperature from the GT equation.

Numerous studies show the importance of crystalline anisotropy on dendrite shapes [25] and growth rate [26]. The capillary and kinetic anisotropy calculated using MD simulations for titanium are $\delta_\varepsilon = 0.0045$ and $\delta_M = 0.021$respectively and, in comparison with those for FCC metals,

these are very small. Given that the spectrum of anisotropy present in various metals and metallic alloys of different crystal structures is pretty large it is important to investigate, in a more general framework, its effect on solidification characteristics such as: solidification morphology, dendrite tip velocity, and mean solidification velocity. Therefore, in this section in addition to the simulations parameterized for titanium we will also explore model systems with anisotropies varying over a large range.

Figure 12 shows the shape of solid-phase generated during solidification by considering titanium and four other model systems at undercoolings of ΔT=100 K and ΔT=250 K. Figures 12 (a) and 12(d) are the morphologies of the simulated systems with anisotropy parameters corresponding to titanium. The other four morphologies correspond to model systems in which alternately one of the anisotropy terms was turned off. The anisotropy parameters were changed separately to study the individual effect of each term on dendrite morphology. Figures 12(a), 12(b), and 12(c) illustrate the effect of the anisotropy parameters on the dendrite shapes for small undercooling of ΔT=100 K. Both the tip radius and the preferred growth direction are affected by the capillary and kinetic anisotropy parameters, δ_ε and δ_M. For the larger undercooling of ΔT=250 K shown in Figures 12 (d), 12(e), and 12(f), the effect of kinetic undercooling on the shape of the dendrites and preferred growth direction is much more pronounced and shows the emergence of side branches in the dendrites. Generation of secondary dendrite arms is related to the thermal diffusion layer thickness which in turn can be estimated as the ratio of thermal diffusivity over interface velocity (D/V). For large undercoolings, the small thermal layer thickness leads to large temperature gradients at the tips of protrusions. When the front of the protrusion faces an undercooled liquid, the heat is dissipated from solid into the liquid. In this case, the protrusion grows and generates side branching. At low undercoolings, the temperature gradient at the tips of protrusions is small, therefore those protrusions cannot survive, and no side branching is observed.

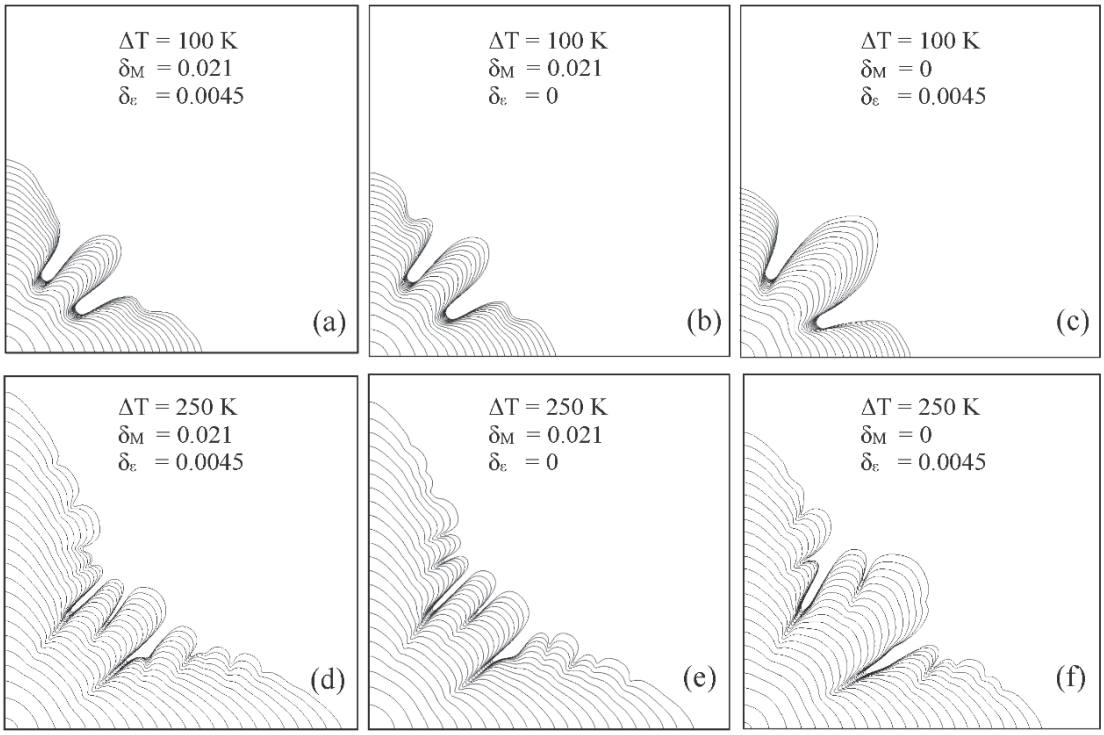

Figure 12: *The effect of capillary, δ_ε, and kinetic, δ_M, anisotropy on dendrite morphology development during solidification in systems at two undercoolings*

Figure 13 shows variation of the tip and average solidification velocities with kinetic anisotropy at undercoolings of ΔT=100 K and ΔT=250 K. The capillary anisotropy was maintained constant at δ_ε=0.0045 while the kinetic anisotropy was varied between δ_M=0 and δ_M=0.08. For both undercoolings, the simulation results show that the increase of δ_M leads to significant increase of the tip velocity while the average solidification velocity increased by only a small amount. Based on Eq. (21), higher kinetic anisotropy leads to a more preferred growth in directions parallel to the x and y-axis directions which in turn increases the tip velocity. When increasing δ_M from 0 to 0.08, at larger undercooling, the tip velocity increases from 16.85 to 23.4 m/s and the average solidification velocity increases from 25.83 and 26.78 m/s. At smaller undercooling when varying δ_M, the tip velocity increases from 1.91 to 2.85 m/s and the average solidification rate increases from 3.28 to 3.62 m/s. These simulation results are in agreement with previous simulations [26] which also show that the effect of kinetic anisotropy is more dominant for large undercoolings.

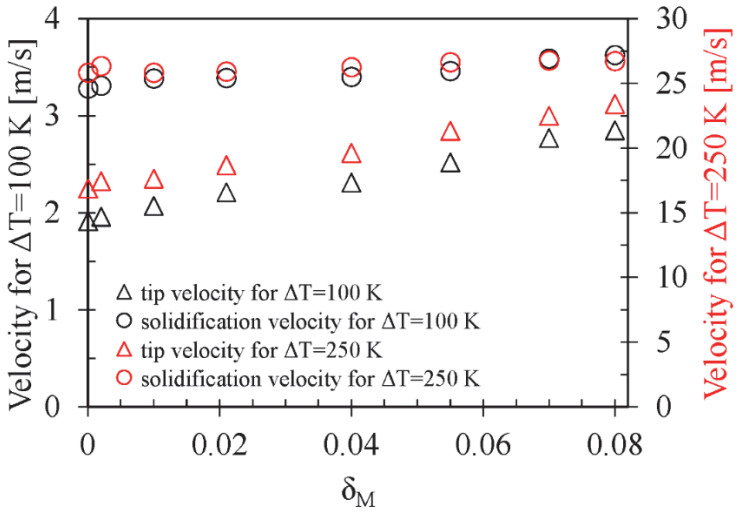

Figure 13: *Variation of the tip and average solidification velocities with kinetic anisotropy at two undercoolings.*

The same analysis is repeated by varying the capillary anisotropy and maintaining the kinetic anisotropy, δ_M=0.021. Figure 14 illustrates the variation of the tip and solidification velocities with capillary anisotropy for two undercoolings. At small undercooling, the increase of δ_ε from 0 to 0.03 increases the tip velocity from 2.1 to 2.76 m/s and increases the average solidification velocity from 3.3 to 3.7 m/s. For larger undercooling, the increase of δ_ε from 0 to 0.03 increases the tip velocity from 18.21 to 20.86 m/s and increases the average solidification velocity from 25.58 and 26.7 m/s. As with kinetic anisotropy, increasing the capillary anisotropy parameter affects the tip velocity more than the average solidification velocity, especially at larger undercoolings.

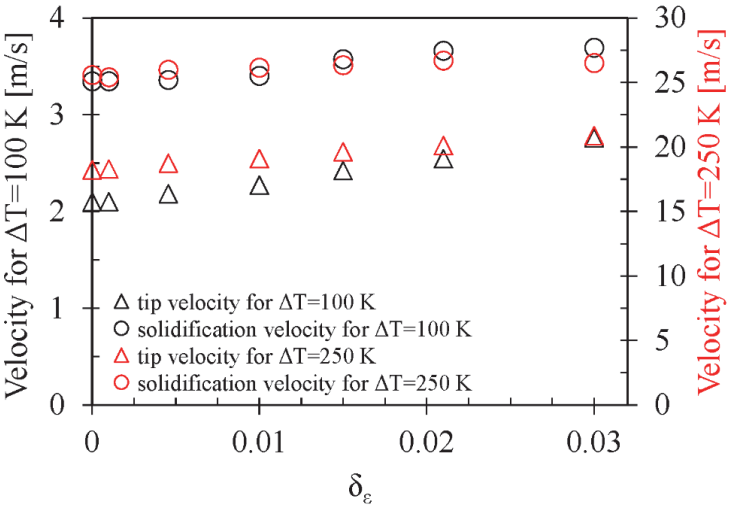

Figure 14: *Variation of the tip and average solidification velocities with capillary anisotropy at two undercoolings.*

4 Conclusions

Solidification of highly undercooled titanium was investigated using a combined MD and phase-field simulation approach. Building on the ongoing developments and applications of atomistic simulation methods to the computation of important thermodynamic and kinetic properties of crystal-melt interfaces in metals, we performed detailed MD calculations of titanium crystal-melt interfacial free energy, kinetic coefficient, and their corresponding anisotropies. Using the MD capillary fluctuation method, the calculated crystal-melt interface free energy of 176 mJ/m^2 is in good agreement with the reported experimental data ranging between 149 and 207 mJ/m^2. By using the free solidification method, implemented based on a multiple layered thermostats approach, the kinetic coefficient calculated is 0.71 m/(s-K). The capillary and kinetic anisotropies obtained from MD simulations are 0.0045 and 0.021 respectively. These MD calculated crystal-melt interfacial properties when combined with the thin interface analysis method provided us with a path for obtaining a subset of the phase-field model parameters that are, in many cases, very difficult to obtain by experimental investigations alone. By adopting the rest of the parameters needed in the model from experiments allowed us to perform parameter-free phase-field simulations of solidification which in turn allowed us to make quantitative comparison between the simulation results and the existing experimental data.

Two slightly different phase-field models were implemented and tested on their ability at predicting the solidification velocity at various undercoolings. For undercoolings below 150K, when using the classical phase-field model, in which the driving force term in the bulk free energy function was considered to vary linearly with undercooling, the simulation and experiment data are in good agreement. However, at larger undercoolings the simulation results show significant deviations from experimental data. By modifying the thermodynamic driving force term in the free energy definition based on the Bragard *et al*. model, the phase-field method not only predicts the solidification velocity consistent with the experiments over a large spectrum of undercoolings, but also provides good estimation of the crystal-melt interface temperature consistent with the Gibbs-Thomson equation. In addition to solidification kinetics, we have studied the effect of anisotropy parameters on the dendritic morphology and growth rate at small and large undercoolings. For both undercoolings, modifications of capillary and kinetic anisotropies affected the dendrite shapes and the tip velocity, while it did not change the solidification velocity

significantly. Moreover, the simulations showed that the effect of capillary anisotropy is larger for small undercoolings, while the kinetic effect becomes more dominant for larger undercoolings.

The results of our study demonstrate that MD simulations combined with phase-field modeling has the potential to provide quantitative, parameter-free, predictions on multiple features characterizing solidification behavior in titanium.

Acknowledgements

The authors gratefully acknowledge the support from the U.S. National Science Foundation (CIMM Project OIA-1541079). The computer resources were provided by LONI and HPC at LSU. M.A.Z. would like to acknowledge the funding support from the U.S. National Science Foundation (NSF-CMMI 1537170 and NSF-CMMI 1855491).

Data availability

The raw/processed data required to reproduce these findings cannot be shared at this time due to technical or time limitations.

References:

[1] F.H. Froes, M.N. Gungor, M.A. Imam, Cost-affordable titanium: The component fabrication perspective, Jom 59(6) (2007) 28-31.
[2] F.H.S. Froes, M.N. Gungor, M. Ashraf Imam, Cost-affordable titanium: The component fabrication perspective, JOM 59(6) (2007) 28-31.
[3] R.R. Boyer, An overview on the use of titanium in the aerospace industry, Materials Science and Engineering: A 213(1) (1996) 103-114.
[4] I.V. Gorynin, Titanium alloys for marine application, Materials Science and Engineering: A 263(2) (1999) 112-116.
[5] I. Gurrappa, Characterization of titanium alloy Ti-6Al-4V for chemical, marine and industrial applications, Materials Characterization 51(2) (2003) 131-139.
[6] T. Traini, C. Mangano, R.L. Sammons, F. Mangano, A. Macchi, A. Piattelli, Direct laser metal sintering as a new approach to fabrication of an isoelastic functionally graded material for manufacture of porous titanium dental implants, Dental Materials 24(11) (2008) 1525-1533.
[7] J.J. Hoyt, M. Asta, A. Karma, Atomistic and continuum modeling of dendritic solidification, Materials Science and Engineering: R: Reports 41(6) (2003) 121-163.
[8] G.J. Fix, Phase field methods for free boundary problems, (1982).
[9] J.S. Langer, MODELS OF PATTERN FORMATION IN FIRST-ORDER PHASE TRANSITIONS, Directions in Condensed Matter Physics, WORLD SCIENTIFIC2013, pp. 165-186.
[10] M. Mamivand, M. Asle Zaeem, H. El Kadiri, L.-Q. Chen, Phase field modeling of the tetragonal-to-monoclinic phase transformation in zirconia, Acta Materialia 61(14) (2013) 5223-5235.
[11] M. Mamivand, M. Asle Zaeem, H. El Kadiri, Phase field modeling of stress-induced tetragonal-to-monoclinic transformation in zirconia and its effect on transformation toughening, Acta Materialia 64 (2014) 208-219.
[12] A. Emdadi, W.G. Fahrenholtz, G.E. Hilmas, M. Asle Zaeem, A modified phase-field model for quantitative simulation of crack propagation in single-phase and multi-phase materials, Engineering Fracture Mechanics 200 (2018) 339-354.
[13] N. Moelans, B. Blanpain, P. Wollants, An introduction to phase-field modeling of microstructure evolution, Calphad 32(2) (2008) 268-294.
[14] S. Ingo, Phase-field models in materials science, Modelling and Simulation in Materials Science and Engineering 17(7) (2009) 073001.
[15] B. Jacob, Z. Mohsen Asle, T. Michael, A phase-field model to study the effects of temperature change on shape evolution of γ -hydrides in zirconium, Journal of Physics D: Applied Physics 49(40) (2016) 405302.
[16] J. Bair, M. Asle Zaeem, D. Schwen, Formation path of δ hydrides in zirconium by multiphase field modeling, Acta Materialia 123 (2017) 235-244.
[17] R. Kobayashi, Modeling and numerical simulations of dendritic crystal growth, Physica D: Nonlinear Phenomena 63(3) (1993) 410-423.
[18] R. Kobayashi, A Numerical Approach to Three-Dimensional Dendritic Solidification, Experimental Mathematics 3(1) (1994) 59-81.
[19] W.J. Boettinger, J.A. Warren, The phase-field method: simulation of alloy dendritic solidification during recalescence, Metallurgical and Materials Transactions A 27(3) (1996) 657-669.

[20] G. Caginalp, Phase Field Models and Sharp Interface Limits: Some Differences in Subtle Situations, Rocky Mountain J. Math. 21(2) (1991) 603-615.
[21] S. Wang, M. Asle Zaeem, M.F. Horstemeyer, P.T. Wang, Investigating thermal effects on morphological evolution during crystallisation of hcp metals: three-dimensional phase field study, Materials Technology 27(5) (2012) 355-363.
[22] O. Penrose, P.C. Fife, Thermodynamically consistent models of phase-field type for the kinetic of phase transitions, Physica D: Nonlinear Phenomena 43(1) (1990) 44-62.
[23] S. Kavousi, D. Moldovan, Phase Field Modeling of Solidification in Single Component Systems, ASME 2017 International Mechanical Engineering Congress and Exposition, American Society of Mechanical Engineers, 2017, pp. V014T11A034-V014T11A034.
[24] A. Karma, W.-J. Rappel, Quantitative phase-field modeling of dendritic growth in two and three dimensions, Physical Review E 57(4) (1998) 4323-4349.
[25] W.J. Boettinger, S.R. Coriell, A.L. Greer, A. Karma, W. Kurz, M. Rappaz, R. Trivedi, Solidification microstructures: recent developments, future directions, Acta Materialia 48(1) (2000) 43-70.
[26] A. Karma, W.-J. Rappel, Numerical Simulation of Three-Dimensional Dendritic Growth, Physical Review Letters 77(19) (1996) 4050-4053.
[27] W.-L. Chan, R.S. Averback, D.G. Cahill, Y. Ashkenazy, Solidification Velocities in Deeply Undercooled Silver, Physical Review Letters 102(9) (2009) 095701.
[28] G.H. Rodway, J.D. Hunt, Thermoelectric investigation of solidification of lead II. Lead alloys, Journal of Crystal Growth 112(2) (1991) 563-570.
[29] M.E. Glicksman, R.J. Schaefer, J.D. Ayers, Dendritic growth-A test of theory, Metallurgical Transactions A 7(11) (1976) 1747-1759.
[30] D.Y. Sun, M. Asta, J.J. Hoyt, Kinetic coefficient of Ni solid-liquid interfaces from molecular-dynamics simulations, Physical Review B 69(2) (2004) 024108.
[31] E. Asadi, M. Asle Zaeem, S. Nouranian, M.I. Baskes, Two-phase solid–liquid coexistence of Ni, Cu, and Al by molecular dynamics simulations using the modified embedded-atom method, Acta Materialia 86 (2015) 169-181.
[32] J.J. Hoyt, M. Asta, Atomistic computation of liquid diffusivity, solid-liquid interfacial free energy, and kinetic coefficient in Au and Ag, Physical Review B 65(21) (2002) 214106.
[33] E. Asadi, M. Asle Zaeem, The anisotropy of hexagonal close-packed and liquid interface free energy using molecular dynamics simulations based on modified embedded-atom method, Acta Materialia 107 (2016) 337-344.
[34] J.J. Hoyt, B. Sadigh, M. Asta, S.M. Foiles, Kinetic phase field parameters for the Cu–Ni system derived from atomistic computations, Acta Materialia 47(11) (1999) 3181-3187.
[35] R. Ramakrishnan, R. Sankarasubramanian, Crystal-melt kinetic coefficients of Ni3Al, Acta Materialia 127 (2017) 25-32.
[36] L. Wu, B. Xu, Q. Li, W. Liu, M. Li, Anisotropic crystal–melt interfacial energy and stiffness of aluminum, Journal of Materials Research 30(11) (2015) 1827-1835.
[37] E. Asadi, M. Asle Zaeem, S. Nouranian, M.I. Baskes, Quantitative modeling of the equilibration of two-phase solid-liquid Fe by atomistic simulations on diffusive time scales, Physical Review B 91(2) (2015) 024105.
[38] W.G. Hoover, B.L. Holian, Kinetic moments method for the canonical ensemble distribution, Physics Letters A 211(5) (1996) 253-257.

[39] Y. Mishin, Calculation of the γ/γ′ interface free energy in the Ni–Al system by the capillary fluctuation method, Modelling and Simulation in Materials Science and Engineering 22(4) (2014) 045001.
[40] M. Asta, J. Hoyt, A. Karma, Calculation of alloy solid-liquid interfacial free energies from atomic-scale simulations, Physical Review B 66(10) (2002) 100101.
[41] Q. Jiang, H.M. Lu, Size dependent interface energy and its applications, Surface Science Reports 63(10) (2008) 427-464.
[42] G.W. Lee, S. Jeon, C. Park, D.-H. Kang, Crystal–liquid interfacial free energy and thermophysical properties of pure liquid Ti using electrostatic levitation: Hypercooling limit, specific heat, total hemispherical emissivity, density, and interfacial free energy, The Journal of Chemical Thermodynamics 63 (2013) 1-6.
[43] S. Walder, P.L. Ryder, A simple technique for the measurement of dendritic growth rates in undercooled metallic melts and its application to Ni and Ti, Materials Science and Engineering: A 203(1) (1995) 197-202.
[44] P. R. Algoso, A. S. Altgilbers, W. Hofmeister, R. J. Bayuzick, The Solidification Velocity of Undercooled Nickel and Titanium Alloys with Dilute Solute, 2003.
[45] J. Bragard, A. Karma, Y.H. Lee, M. Plapp, Linking Phase-Field and Atomistic Simulations to Model Dendritic Solidification in Highly Undercooled Melts, Interface Science 10(2) (2002) 121-136.
[46] W.-S. Ko, B. Grabowski, J. Neugebauer, Development and application of a Ni-Ti interatomic potential with high predictive accuracy of the martensitic phase transition, Physical Review B 92(13) (2015) 134107.
[47] Y.-M. Kim, B.-J. Lee, M.I. Baskes, Modified embedded-atom method interatomic potentials for Ti and Zr, Physical Review B 74(1) (2006) 014101.
[48] R.G. Hennig, T.J. Lenosky, D.R. Trinkle, S.P. Rudin, J.W. Wilkins, Classical potential describes martensitic phase transformations between the α, β, and ω titanium phases, Physical Review B 78(5) (2008) 054121.
[49] M. Mendelev, T. Underwood, G. Ackland, Development of an interatomic potential for the simulation of defects, plasticity, and phase transformations in titanium, The Journal of chemical physics 145(15) (2016) 154102.
[50] J.J. Valencia, Thermophysical properties, Modeling for Casting and Solidification Processing 189 (2001).
[51] E. Asadi, M. Asle Zaeem, S. Nouranian, M.I. Baskes, Quantitative modeling of the equilibration of two-phase solid-liquid Fe by atomistic simulations on diffusive time scales, Physical Review B 91(2) (2015) 024105.
[52] D. Holland-Moritz, O. Heinen, R. Bellissent, T. Schenk, Short-range order of stable and undercooled liquid titanium, Materials Science and Engineering: A 449–451 (2007) 42-45.
[53] B.G. del Rio, O. Rodriguez, L.E. González, D.J. González, First principles determination of static, dynamic and electronic properties of liquid Ti near melting, Computational Materials Science 139 (2017) 243-251.
[54] B. Lee, G.W. Lee, Local structure of liquid Ti: Ab initio molecular dynamics study, The Journal of Chemical Physics 129(2) (2008) 024711.
[55] S. Plimpton, Fast Parallel Algorithms for Short-Range Molecular Dynamics, Journal of Computational Physics 117(1) (1995) 1-19.
[56] F. Celestini, J.-M. Debierre, Measuring kinetic coefficients by molecular dynamics simulation of zone melting, Physical Review E 65(4) (2002) 041605.

[57] J. Monk, Y. Yang, M.I. Mendelev, M. Asta, J.J. Hoyt, D.Y. Sun, Determination of the crystal-melt interface kinetic coefficient from molecular dynamics simulations, Modelling and Simulation in Materials Science and Engineering 18(1) (2010) 015004.
[58] C.L. Kelchner, S.J. Plimpton, J.C. Hamilton, Dislocation nucleation and defect structure during surface indentation, Physical Review B 58(17) (1998) 11085-11088.
[59] M. Newville, T. Stensitzki, D. B. Allen, A. Ingargiola, LMFIT: Non-Linear Least-Square Minimization and Curve-Fitting for Python¶, 2014.
[60] J.Q. Broughton, G.H. Gilmer, Molecular dynamics of the crystal–fluid interface. V. Structure and dynamics of crystal–melt systems, The Journal of Chemical Physics 84(10) (1986) 5749-5758.
[61] X.-M. Bai, M. Li, Calculation of solid-liquid interfacial free energy: A classical nucleation theory based approach, The Journal of Chemical Physics 124(12) (2006) 124707.
[62] S. Angioletti-Uberti, M. Ceriotti, P.D. Lee, M.W. Finnis, Solid-liquid interface free energy through metadynamics simulations, Physical Review B 81(12) (2010).
[63] D. Şopu, J. Rogal, R. Drautz, Thermodynamic and kinetic solid-liquid interface properties from transition path sampling, The Journal of Chemical Physics 145 (2016) 244703.
[64] J.R. Espinosa, C. Vega, E. Sanz, The mold integration method for the calculation of the crystal-fluid interfacial free energy from simulations, The Journal of Chemical Physics 141(13) (2014) 134709.
[65] U.R. Pedersen, Direct calculation of the solid-liquid Gibbs free energy difference in a single equilibrium simulation, The Journal of Chemical Physics 139(10) (2013) 104102.
[66] J.J. Hoyt, M. Asta, A. Karma, Method for Computing the Anisotropy of the Solid-Liquid Interfacial Free Energy, Physical Review Letters 86(24) (2001) 5530-5533.
[67] C. A. Becker, D. L. Olmsted, M. Asta, J. Hoyt, S.M. Foiles, Atomistic simulations of crystal-melt interfaces in a model binary alloy: Interfacial free energies, adsorption coefficients, and excess entropy, 2009.
[68] N. Provatas, K. Elder, Phase-field methods in materials science and engineering, John Wiley & Sons2011.
[69] S.G. Kim, W.T. Kim, J.S. Lee, M. Ode, T. Suzuki, Large Scale Simulation of Dendritic Growth in Pure Undercooled Melt by Phase-field Model, ISIJ International 39(4) (1999) 335-340.
[70] J. Lipton, W. Kurz, R. Trivedi, Rapid dendrite growth in undercooled alloys, Acta Metallurgica 35(4) (1987) 957-964.
[71] J. Kierzenka, L.F. Shampine, A BVP solver based on residual control and the Maltab PSE, ACM Transactions on Mathematical Software (TOMS) 27(3) (2001) 299-316.